

# Relation between speckle decorrelation and optical phase conjugation (OPC)-based turbidity suppression through dynamic scattering media: a study on *in vivo* mouse skin

Mooseok Jang,<sup>1,5</sup> Haowen Ruan,<sup>1,5</sup> Ivo M. Vellekoop,<sup>2</sup> Benjamin Judkewitz,<sup>3</sup>  
Euiheon Chung,<sup>4,6</sup> and Changhui Yang<sup>1,\*</sup>

<sup>1</sup>Department of Electrical Engineering, California Institute of Technology, 1200 E. California Boulevard, Pasadena, California, 91125 USA

<sup>2</sup>MIRA Institute for Biomedical Technology and Technical Medicine, University of Twente, P.O. Box 217, 7500 AE Enschede, The Netherlands

<sup>3</sup>NeuroCure Cluster of the German Excellence Initiative, Charité Berlin, Charitéplatz. 1, 10117 Berlin, Germany

<sup>4</sup>Department of Medical System Engineering and School of Mechatronics, Gwangju Institute of Science and Technology, Gwangju 500-712 South Korea

<sup>5</sup>These authors contributed equally to this paper

<sup>6</sup>Co corresponding authors: E.C. (ogong50@gist.ac.kr)

\*C.Y. (chyang@caltech.edu)

**Abstract:** Light scattering in biological tissue significantly limits the accessible depth for localized optical interrogation and deep-tissue optical imaging. This challenge can be overcome by exploiting the time-reversal property of optical phase conjugation (OPC) to reverse multiple scattering events or suppress turbidity. However, in living tissue, scatterers are highly movable and the movement can disrupt time-reversal symmetry when there is a latency in the OPC playback. In this paper, we show that the motion-induced degradation of the OPC turbidity-suppression effect through a dynamic scattering medium shares the same decorrelation time constant as that determined from speckle intensity autocorrelation – a popular conventional measure of scatterer movement. We investigated this decorrelation characteristic time through a 1.5-mm-thick dorsal skin flap of a living mouse and found that it ranges from 50 ms to 2.5 s depending on the level of immobilization. This study provides information on relevant time scales for applying OPC to living tissues.

©2014 Optical Society of America

**OCIS codes:** (070.5040) Phase conjugation; (170.7050) Turbid media; (190.5040) Phase conjugation; (090.1995) Digital holography; (110.1080) Active or adaptive optics.

## References and links

1. A. Yariv, "Phase Conjugate Optics and Real-Time Holography," *IEEE J. Quantum Electron.* **14**(9), 650–660 (1978).
2. Z. Yaqoob, D. Psaltis, M. S. Feld, and C. Yang, "Optical Phase Conjugation for Turbidity Suppression in Biological Samples," *Nat. Photonics* **2**(2), 110–115 (2008).
3. E. J. McDowell, M. Cui, I. M. Vellekoop, V. Senekerimyan, Z. Yaqoob, and C. Yang, "Turbidity suppression from the ballistic to the diffusive regime in biological tissues using optical phase conjugation," *J. Biomed. Opt.* **15**(2), 025004 (2010).
4. X. Xu, H. Liu, and L. V. Wang, "Time-reversed ultrasonically encoded optical focusing into scattering media," *Nat. Photonics* **5**(3), 154–157 (2011).
5. Y. M. Wang, B. Judkewitz, C. A. Dimarzio, and C. Yang, "Deep-tissue focal fluorescence imaging with digitally time-reversed ultrasound-encoded light," *Nat. Commun.* **3**, 928 (2012).
6. K. Si, R. Fiolka, and M. Cui, "Fluorescence imaging beyond the ballistic regime by ultrasound pulse guided digital phase conjugation," *Nat. Photonics* **6**(10), 657–661 (2012).
7. H. Ruan, M. Jang, B. Judkewitz, and C. Yang, "Iterative Time-Reversed Ultrasonically Encoded Light Focusing in Backscattering Mode," *Sci. Rep.* **4**, 7156 (2014).
8. C. L. Hsieh, Y. Pu, R. Grange, and D. Psaltis, "Digital phase conjugation of second harmonic radiation emitted by nanoparticles in turbid media," *Opt. Express* **18**(12), 12283–12290 (2010).

9. I. M. Vellekoop, M. Cui, and C. Yang, "Digital optical phase conjugation of fluorescence in turbid tissue," *Appl. Phys. Lett.* **101**(8), 081108 (2012).
10. M. Cui, E. J. McDowell, and C. Yang, "An in vivo study of turbidity suppression by optical phase conjugation (TSOPC) on rabbit ear," *Opt. Express* **18**(1), 25–30 (2010).
11. M. Cui and C. Yang, "Implementation of a digital optical phase conjugation system and its application to study the robustness of turbidity suppression by phase conjugation," *Opt. Express* **18**(4), 3444–3455 (2010).
12. I. M. Vellekoop and C. M. Aegerter, "Focusing light through living tissue," in *Proceedings of SPIE*, J. A. Izatt, J. G. Fujimoto, and V. V. Tuchin, eds. (2010), **Vol. 7554**, p. 755430.
13. E. Cuche, P. Marquet, and C. Depeursinge, "Spatial filtering for zero-order and twin-image elimination in digital off-axis holography," *Appl. Opt.* **39**(23), 4070–4075 (2000).
14. M. Jang, H. Ruan, H. Zhou, B. Judkewitz, and C. Yang, "Method for auto-alignment of digital optical phase conjugation systems based on digital propagation," *Opt. Express* **22**(12), 14054–14071 (2014).
15. V. Viasnoff, F. Lequeux, and D. J. Pine, "Multispeckle diffusing-wave spectroscopy: A tool to study slow relaxation and time-dependent dynamics," *Rev. Sci. Instrum.* **73**(6), 2336 (2002).
16. P. Lemieux and D. Durian, "Investigating non-Gaussian scattering processes by using n th-order intensity correlation functions," *J. Opt. Soc. Am. A* **16**(7), 1651–1664 (1999).
17. E. Cuche, P. Marquet, and C. Depeursinge, "Spatial filtering for zero-order and twin-image elimination in digital off-axis holography," *Appl. Opt.* **39**(23), 4070–4075 (2000).
18. S. T. Flock, S. L. Jacques, B. C. Wilson, W. M. Star, and M. J. van Gemert, "Optical properties of Intralipid: a phantom medium for light propagation studies," *Lasers Surg. Med.* **12**(5), 510–519 (1992).
19. R. Samatham, S. L. Jacques, and P. Campagnola, "Optical properties of mutant versus wild-type mouse skin measured by reflectance-mode confocal scanning laser microscopy (rCSLM)," *J. Biomed. Opt.* **13**(4), 041309 (2008).
20. S. L. Jacques, "Optical properties of biological tissues: a review," *Phys. Med. Biol.* **58**(11), R37–R61 (2013).
21. J. H. Kregel, J. B. Hodgins, J. R. Hagaman, and O. Smithies, "A noninvasive computerized tail-cuff system for measuring blood pressure in mice," *Hypertension* **25**(5), 1111–1115 (1995).
22. D. J. Pine, D. A. Weitz, P. M. Chaikin, and E. Herbolzheimer, "Diffusing wave spectroscopy," *Phys. Rev. Lett.* **60**(12), 1134–1137 (1988).
23. A. Ewald, Z. Werb, and M. Egeblad, "Monitoring of vital signs for long-term survival of mice under anesthesia," *Cold Spring Harb. Protoc.* **2011**, (2011).
24. T. Laforest and A. Dupret, "A 4000 Hz CMOS image sensor with in-pixel processing for light measurement and modulation," *New Circuits Syst. Conf. IEEE 11th Int.* 1–4 (2013).

## 1. Introduction

Optical phase conjugation (OPC) is the process whereby an incoming light field is reproduced and played back in the backward direction such that the phase-conjugated light beam corresponds to a time-reversed input beam [1]. For biomedical applications, this time-reversal property can be used to increase the accessible depth of light inside biological tissue by cancelling out multiple scattering (Fig. 1, right top) [2,3].

The concept of turbidity suppression of biological tissue by optical phase conjugation was first demonstrated in 2008 with 0.69-mm-thick chicken breast tissue in which the mean number of photon scattering events was approximately 26 [2]. A subsequent experimental demonstration was performed through chicken breast tissue that was up to 7 mm thick [3]. The turbidity-suppression technique has also enabled light focusing inside scattering media by virtually or physically placing a guide-star (e.g., ultrasonic light modulation [4–7], second-harmonic-generation-active nanomaterial [8], or a fluorescent bead with a narrow bandwidth filter [9]) within deep tissue.

The OPC-based turbidity suppression technique has been performed in two sequential steps: wavefront recording and playback. In early demonstrations, a photorefractive medium was used for the holographic recording and readout [2,3,10]. However, in biomedical applications such as fluorescence imaging and photodynamic therapy, its application is limited by its low OPC amplification, which is defined by the power ratio between the phase-conjugated beam and the input signal beam. In 2010, digital OPC (DOPC)-based turbidity suppression was implemented with two independent digital components, a wavefront sensor and a spatial light modulator, to achieve higher OPC amplification (arbitrary amplification, in principle) [11]. In the DOPC system, wavefront recording is performed using phase-shifting interferometry or off-axis interferometry (Fig. 1, left). The conjugated copy of the measured wavefront is then computed and played back on the spatial light modulator (Fig. 1, right top).

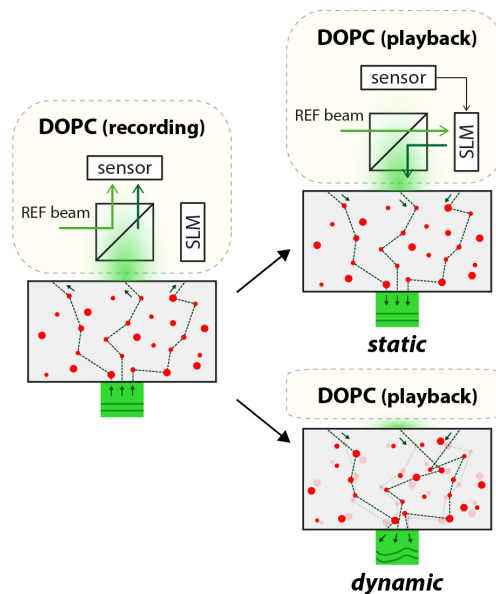


Fig. 1. DOPC process through moving scatterers. As the first step of the DOPC process, the signal light beam (collimated beam) is incident on the multiple-scattering sample and its disordered wavefront is recorded from the sensor on the other side of the sample (left). Then, if the scatterers' configuration is static during the DOPC process – wavefront calculation and playback on the spatial light modulator (SLM) – the OPC beam retraces the original scattering trajectories, which in turn reconstructs the signal light field from the opposite side (right top). However, if the scatterers move during the DOPC process, the time-reversal symmetry is broken so that the OPC beam cannot retrace its original trajectory. Thus, the original signal light field is not properly reconstructed (right bottom).

Despite these technical developments, *in vivo* application of the turbidity suppression technique remains quite limited. The primary obstacle is the movement of scatterers inside tissue caused by essential physiological processes such as blood flow/pulsation, breathing and the tissues' fluidic environment. More specifically, when movement significantly changes the configuration of scatterers in the time interval between OPC wavefront recording and playback, the time symmetry is broken and the turbidity suppression effect is diminished (Fig. 1, right bottom).

Most of the OPC-based experimental demonstrations to date have only been performed with a mixture of polystyrene beads or *in vitro* samples such as chicken tissue sections. To our knowledge, the only live tissue study reported thus far was an early experiment in which a clamped live rabbit ear was used [10]. However, this experiment was limited in a couple of ways. First, turbidity suppression was demonstrated through a tightly-clamped ear and therefore most of the blood circulation inside the tissue was blocked off. Second, the latency of the OPC technique was as high as  $\sim 5$  s, since the OPC playback in that experiment was generated using a photorefractive crystal, which is slow to record and read out. The latter deficiency was particularly significant because it prevented any observation of turbidity suppression effects that have fast decorrelation time constants. An approach has been developed to iteratively optimize the wavefront to suppress turbidity and focusing through living *Drosophila melanogaster* pupae [12]. However, given the number of controlling optical modes, this type of feedback-based adaptive optics method is not an optimal way to deal with fast scatterer movement.

In this study, we aim to show theoretically and experimentally that the degradation of OPC turbidity suppression shares the same decorrelation characteristic as the speckle intensity autocorrelation. We achieved 100 ms DOPC system latency by employing off-axis holography [13] for single-shot wavefront measurement and fast graphics processing unit (GPU) computation of the optical phase. Using the fast system (overall 200 ms system latency

with the auto-alignment method [14]), we observed the equivalence between the fidelity of turbidity suppression and speckle intensity autocorrelation with tissue phantoms decorrelating at various time scales ranging from 50 ms to ~10 s. We then investigated the decorrelation characteristic of 1.5-mm-thick dorsal skin of a living mouse at different levels of immobilization and found that it ranged from 50 ms to 2 s. Furthermore, we found that turbidity suppression can be achieved even at an extremely low-intensity autocorrelation (<0.05) albeit its contrast is reduced correspondingly.

## 2. Theory

In this section, we define two quantities: the speckle intensity autocorrelation function and the fidelity of OPC turbidity suppression, and we derive their theoretical equivalence. First, the normalized speckle intensity autocorrelation function, the correlation between speckle patterns at time  $t_0$  and  $t_0 + \tau$ , is calculated from the temporal sequence of multi-speckle images captured from the camera [15]:

$$g_2(\tau) \equiv \frac{\sum_m I_m(t_0)I_m(t_0 + \tau) / M}{\sum_m I_m(t_0) / M \sum_m I_m(t_0 + \tau) / M} - 1 \quad (1)$$

where  $I_m(t)$  is the intensity of the transmitted scattered light, as recorded by the  $m_{th}$  pixel of the sensor at time  $t$  and  $M$  is the total number of pixels on the sensor.  $t_0$  is the reference time at which the OPC wavefront is recorded. Here,  $g_2(\tau)$  ranges from 0 to 1 as the "-1" term is appended [15]. In our experiment, the time-lapse speckle pattern is captured in transmission geometry (with the signal beam). Assuming that the average transmittance does not change over time ( $\bar{I} = \bar{I}(t_0) = \bar{I}(t_0 + \tau)$ ), Eq. (1) is simplified to

$$g_2(\tau) \equiv \frac{\sum_m I_m(t_0)I_m(t_0 + \tau) / M}{\bar{I}^2} - 1. \quad (2)$$

where  $\bar{I}(t)$  is the average intensity,  $\sum_m I_m(t) / M$ . Assuming the scattering process is ergodic, this equation can be written in the ensemble-averaged form [15]:

$$g_2(\tau) \equiv \frac{\langle I(t_0)I(t_0 + \tau) \rangle}{\langle I \rangle^2} - 1. \quad (3)$$

On the other hand, the fidelity of OPC turbidity suppression is quantified by the intensity of the phase-conjugated beam returning to the original input mode. In our experiment, the signal beam (input) was collimated. Thus, the time-reversed beam would also be collimated after it has counter-propagated through the scattering media. We measured the intensity of the time-reversed beam on the input side of the sample (where the signal beam entered) by focusing it on the avalanche photodiode (APD). We refer to the spot being focused on as the OPC spot. The OPC system records the wavefront at time  $t_0$ , and after some latency  $\tau$ , it displays the phase conjugated wavefront. Using a transmission matrix formulation, the OPC spot intensity is (assuming an input intensity of unity)

$$I_{OPC}(\tau) = A \frac{\left| \sum_m T_m(t_0 + \tau) T_m^*(t_0) \right|^2}{\left| \sum_m T_m(t_0) T_m^*(t_0) \right|^2} \quad (4)$$

where  $A$  is the OPC amplification. Thus, if there is no latency ( $\tau = 0$ ), the reconstructed input mode has an intensity of  $A$ .  $T_m(t)$  is the transmission matrix component relating the electric field of the original input mode to the transmitted electric field at the  $m_{th}$  pixel on the OPC plane. The same transmission matrix component governs the field propagation in the reverse direction –from the OPC plane to the input side of the sample – due to the time-reversal symmetry of the scattering events. The transmission matrix component varies temporally because we assume that a dynamic sample was used. Then, we define the turbidity suppression fidelity as

$$F(\tau) = \frac{I_{OPC}(\tau)}{I_{OPC}(0)}. \quad (5)$$

The normalization term,  $I_{OPC}(0)$ , is the intensity of the OPC spot that would be obtained with a perfectly static sample. In our study, we experimentally determined the normalization factor by measuring the OPC spot intensity through the fully-cured tissue phantom (for the first part of the experiment) and the euthanized mouse (for the second part of the experiment).

To show the equivalence between  $g_2(\tau)$  and  $F(\tau)$ , we use the Siegert relation [16]:

$$g_2(\tau) = \beta |g_1(\tau)|^2. \quad (6)$$

which relates the intensity autocorrelation function to the field autocorrelation function,  $g_1(\tau)$ .  $\beta$  is an experimental constant, which is ideally 1 [16]. The constant accounts for the reduction in speckle contrast due to various factors, such as the number of sensor pixels per speckle and system noise [15,16].

Here,  $g_1(\tau)$ , the field autocorrelation function, is given by

$$g_1(\tau) = \frac{\sum_m E_m^*(t_0)E_m(t_0 + \tau)}{\sqrt{\sum_m E_m^*(t_0)E_m(t_0)}\sqrt{\sum_m E_m^*(t_0 + \tau)E_m(t_0 + \tau)}} \quad (7)$$

where  $E_m(t)$  is the field of the transmitted scattered light at the  $m_{th}$  pixel of the sensor. With the assumption used above – time-invariance of average transmittance, the field autocorrelation function is

$$g_1(\tau) \equiv \frac{\sum_m T_m^*(t_0)T_m(t_0 + \tau)}{\sum_m T_m^*(t_0)T_m(t_0)}. \quad (8)$$

Using the Eqs. (4), (5) and (8) we then get:

$$F(\tau) = |g_1(\tau)|^2. \quad (9)$$

From Eqs. (6) and (9), the speckle intensity autocorrelation function is proportional to the normalized OPC spot intensity:

$$g_2(\tau) = \beta F(\tau). \quad (10)$$

Since  $F(0) = 1$  by definition,  $\beta$  can be determined experimentally from the captured speckle pattern using the relation  $\beta = g_2(0)$ . It ranged from 0.8 to 1.0. Such high experimental values of  $g_2(0)$  indicate that the camera exposure (9 ms in our case) is much faster than the sample dynamics. If the camera exposure is comparable to or slower than the scatterer movement,

each pixel on the sensor integrates a temporal sequence of independent speckle fields so that the value of  $g_2(0)$  that is effectively measured will be reduced. The temporal integration of many speckle fields will also correspondingly degrade the turbidity suppression fidelity  $F(\tau)$  because the wavefront measured for the optical phase conjugation will be blurred.

### 3. Relation between the speckle decorrelation and the OPC-based turbidity suppression

#### 3.1. Experimental setup

We first performed a synchronized measurement of the speckle intensity autocorrelation,  $g_2(t)$ , and the turbidity suppression fidelity,  $F(\tau)$ , to show the equivalence between them. This set of experiment is performed with tissue phantoms and we will describe the details of the experimental scheme in this section.

Figure 2 shows the experimental setup. We used a 150-mW, 532-nm diode-pumped solid-state laser as the light source. The laser beam is split into two beam paths: the signal beam and the reference beam. The signal beam is split into two paths for the digital OPC procedure and the speckle decorrelation measurement. Each signal beam has an intensity of  $\sim 5$  mW and its beam waist is  $\sim 1$  mm. Figure 2(a) shows the beam paths for the OPC wavefront measurement. One of the signal beams is propagated through the scattering medium (here, a tissue phantom) and is guided to the sCMOS camera (pco.edge 5.5, PCO) through a 1X telescope system composed of a pair of 15-cm focal length plano-convex lenses. The telescope system optically conjugates the DOPC plane to the back-focal plane of the signal collecting lens (2.5-cm focal length plano-convex lens). By obliquely guiding ( $\sim 1.8^\circ$ ) the signal beam to the sensor plane (while the collimated reference beam is normally incident), we are able to use the off-axis holographic method. Thus, we calculate the signal beam's wavefront from a single interferogram which is captured from the sCMOS camera (sCMOS1) [17]. The speckle size of the signal beam is set to  $\sim 6 \times 6$  and the camera's ROI is  $1920 \times 1080$ . In turn, we measure and conjugate the phase of around 50,000 optical modes.

Figure 2(b) shows the beam paths for the OPC playback. A phase-conjugated copy of the measured wavefront is displayed on the phase-only spatial light modulator (PLUTO phase only, Holoeye); Next the SLM-reflected reference beam (OPC beam) retraces the signal beam's original scattering trajectories (Fig. 2 (b)) and leaves the sample as a collimated beam that is directed onto an APD (SPCM-AQRH-14, PerkinElmer) and a CCD sensor (pixelfly qe, PCO). We quantified the turbidity suppression fidelity from the OPC beam intensity measured from the APD. The CCD is used to directly confirm the presence of the OPC spot.

The latency of the DOPC system – the time required for the wavefront measurement (30 ms), data processing (30 ms), and display on the SLM (30ms) – is around 100 ms. The off-axis configuration reduces the time for the wavefront measurement as it requires a single interferogram for a wavefront measurement. However, compared to the phase-stepping methods, it measures a smaller number of optical modes. Because the off-axis methods involve the Fourier transform as well as an inverse Fourier transform of a large matrix ( $1920 \times 1080$ ), the computation load was significant. Therefore we used a high-end GPU (GeForce GTX TITAN, NVIDIA) to enhance the data processing speed. In this study, we employed a digital auto-alignment method to maximize the DOPC performance which requires an additional 100 ms of computation time [14]. The overall system latency is therefore around 200 ms.

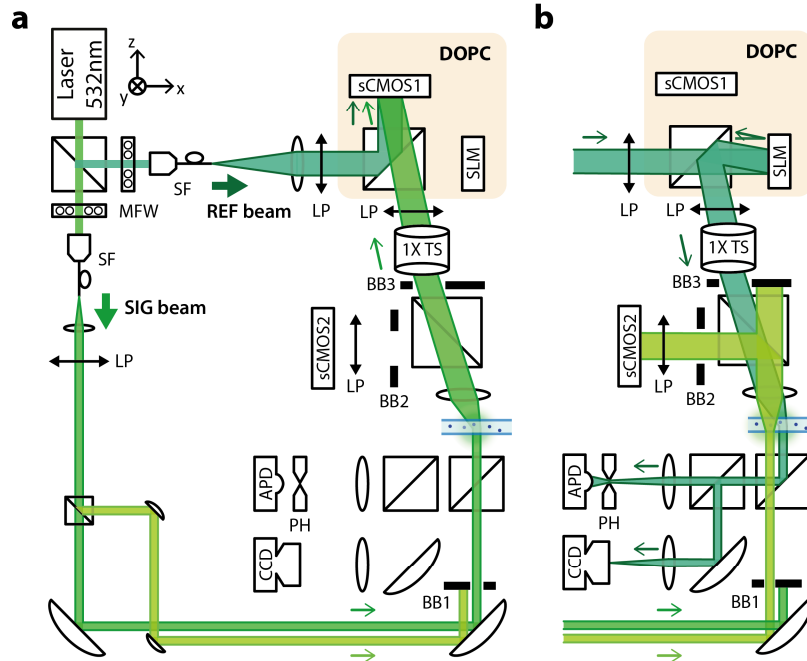


Fig. 2. Experimental setup. (a) The experimental setup used for the tissue phantom and the beam paths used for wavefront measurement. The laser beam is split into two beam paths: the signal beam and reference beam. Both beams are spatially filtered through the single mode fiber and collimated. The reference beam is normally incident on both SCMOS sensor (sCMOS1) and SLM. The signal beam is split into two paths – one for the speckle autocorrelation measurement and one for the DOPC procedure. The signal beam for the DOPC procedure propagates through the tissue phantom and is obliquely guided ( $1.8^\circ$ ) on the sensor plane so that we are able to use the off-axis holographic method. BB1 blocks the signal beam for speckle measurement at this step. (b) The experimental setup and beam paths used for the synchronized measurement of the speckle autocorrelation function and OPC spot intensity. The laser source, spatial filters, collimation lens shown in (a) are omitted. The phase-conjugated copy of the measured wavefront is displayed on the SLM. Next the reconstructed OPC beam, which is collimated as it propagates through the dorsal skin, is measured from the APD and the CCD. The signal beam for the DOPC procedure (shown in (a)) was blocked while monitoring the intensity of the OPC beam. A  $50\text{-}\mu\text{m}$  pinhole was placed in front of the APD to allow only the phase-conjugated mode. Three beam blockers are in place to block unwanted back-reflections that would prevent synchronized measurement. BB1 blocks the signal beam for the DOPC procedure after the OPC wavefront is recorded so that its back-reflected portion does not interfere with the OPC beam at the APD. BB2 blocks the back-reflection of the OPC beam to the sCMOS camera capturing the transmitted speckle pattern. BB3 blocks the signal beam for speckle measurement from entering into the DOPC system. SF = spatial filter; 1X TS = 1X telescope; PH = pinhole; BB = beam block; MFW = motorized filter wheel; LP = linear polarizer; SLM = spatial light modulator; sCMOS = scientific CMOS camera; CCD = CCD camera; APD = avalanche photodiode.

Because light transmittance through scattering media is low, we adjust the motorized filter wheel (FW103, Thorlabs) to switch the light intensity between the phase recording and the playback. When we play back the phase-conjugated beam, we increase the reference light intensity so that we can clearly measure the reconstructed input mode from the other side of the scattering medium. When we record the wavefront, we decrease the reference light with the motorized filter wheel so that we do not saturate the camera pixels. For the off-axis methods, we set the intensity ratio between the reference beam and the signal beam to roughly 5:1.

During the DOPC procedure, the other signal beam path, which is not used for the DOPC procedure, is guided to the sCMOS2 through the scattering media. sCMOS2 simultaneously captures the time-lapse multi-speckle pattern from which we calculate the speckle

autocorrelation function. The speckle size is  $\sim 6 \times 6$  pixels and the camera's region of interest is  $160 \times 160$ . Statistical stability is assured by the large number of speckles ( $\sim 700$  speckles). The exposure time and frame per second is set to 9 ms and 100, respectively. Because the beam paths for the DOPC procedure and speckle decorrelation measurement are spatially separated, we can block the problematic back-reflections and observe the clear speckle pattern with the sCMOS camera on one side of the sample while simultaneously observing the OPC spot with the CCD camera and the APD on the other side of the sample. This approach is only valid when the sample's dynamics are spatially homogenous as we have employed two different beam paths. Therefore we are able to perform the synchronized measurement with an artificial-tissue phantom.

### 3.2. Result

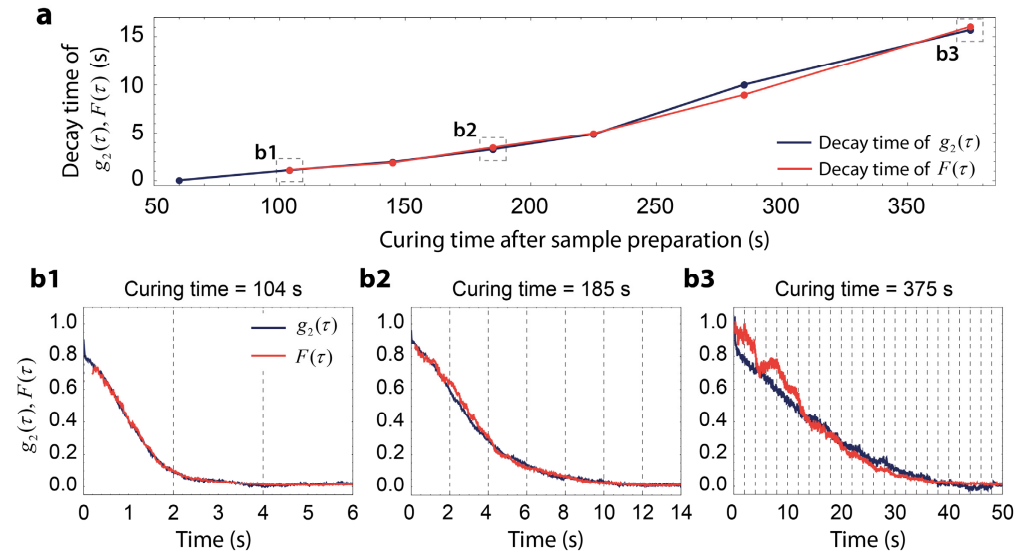


Fig. 3. Simultaneously-measured speckle intensity autocorrelation function and the OPC spot intensity through a tissue phantom. (a)  $1/e$  decay time of the speckle intensity autocorrelation function and OPC spot intensity. As gel is cured at room temperature, the decay time becomes longer. This shows that the degradation of the OPC turbidity suppression shares the same time constant as the speckle decorrelation. For the first measurement, after 60 s of curing time, the OPC decay time could not be measured because the decorrelation is faster than the system latency. (b1-b3) The speckle autocorrelation function (blue) and the turbidity suppression (red) at different curing times: the time axis in b1, b2 and b3 are referenced at the curing time of 104 s, 185 s and 375 s respectively. For different time scales, the two curves show close agreement in the time characteristic. In b3, greater fluctuation in the OPC spot intensity and the speckle autocorrelation function are observed as a result of the interference between the stable portion (changing slowly) and the decorrelating portion of the sample-transmitted light field.

The 3.5-mm-thick tissue phantom sample was made with 1% agar gel (Invitrogen) with 2% Intralipid (Invitrogen). The corresponding scattering/absorption coefficient and anisotropy constant is  $10 \text{ mm}^{-1}$ ,  $0.002 \text{ mm}^{-1}$ , and 0.85, respectively [18]. We mixed the Intralipid with the agar in an aqueous phase and performed several sets of synchronized measurements before the gel was completely cured. Figure 3(a) shows the decay time of the speckle intensity autocorrelation function (blue line) and the OPC turbidity suppression fidelity (red line) measured over the course of curing. Here, the decay time is defined as the time in which the speckle autocorrelation function and the turbidity suppression fidelity drops to  $1/e$ . The decay time becomes longer as the gel solidifies. As theoretically derived, we observed a good match between the two time constants. The profile of turbidity suppression fidelity shows a significant match to the profile of speckle autocorrelation function in various time scales as

well (Fig. 3(b)). Each curve from the synchronized measurement is referenced at a different curing time (104 s, 185 s and 375 s). Because of the DOPC system latency and the computation time required for digital auto-alignment, the OPC spot intensity is observed ~200 ms after the wavefront measurement.

#### 4. Decorrelation characteristic of the dorsal skin of a live mouse

##### 4.1. Experimental setup

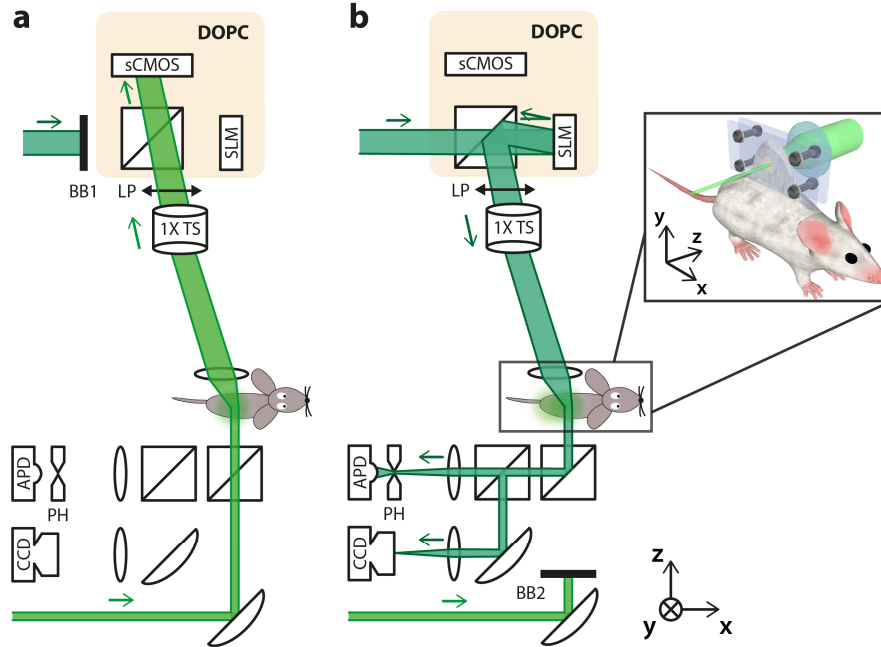


Fig. 4. Experimental setup. The laser source, spatial filters, collimation lens shown in Fig. 2 are omitted. (a) The experimental setup used for the mouse dorsal skin flap and the beam paths used for the speckle measurement. The signal beam path used for the DOPC procedure was used for speckle measurement as well for the mouse dorsal skin flap. The time-lapse speckle pattern is measured with the sCMOS camera in the DOPC system. The reference beam is blocked. (b) The experimental setup and beam paths used for the measurement of the OPC spot intensity. The signal beam wavefront is measured using the off-axis holographic method described in Fig. 2(a). The phase-conjugated copy of the measured wavefront is displayed on the SLM. The reconstructed OPC beam is measured from the APD and the CCD. The inset shows the mouse dorsal skin flap model we used. We pinched mouse dorsal skin with two acrylic plates secured by four bolts and nuts. The speckle intensity autocorrelation function and the OPC spot are measured with three different configurations. 1X TS = 1X telescope; PH = pinhole; BB = beam block; LP = linear polarizer; SLM = spatial light modulator; sCMOS = scientific CMOS camera; CCD = CCD camera; APD = avalanche photodiode.

We characterized the speckle decorrelation time of the mouse dorsal skin flap with three different configurations: 1) a laser beam incident on the skin flap (~1.5 mm thick) pinched by a pressure of ~5 psi, 2) the skin flap where its surrounding region is pinched by a pressure of ~5 psi, and 3) the unclamped skin with minimal immobilization. We also reconstructed the OPC spot and measured its intensity decay. However, because the synchronized measurement setup (in Fig. 2) is not valid for the spatially inhomogeneous sample (the mouse dorsal skin flap), we separately measured the speckle autocorrelation and the OPC spot intensity. All of these procedures were approved by the Institutional Animal Care and Use Committee at the California Institute of Technology.

Figure 4 shows the experimental setup. First, to measure the speckle intensity autocorrelation, the time-lapse multi-speckle pattern is captured from the sCMOS camera

while blocking the reference beam (Fig. 4(a)). For the measurement of the turbidity suppression fidelity, we generated the time-reversed beam using the same procedure as described in Section 3.1 and monitored the OPC spot intensity with the APD as shown in Fig. 4(b). The measurement parameters, including the speckle size, exposure time and frame rate, are the same parameters we used in the experiment with the artificial tissue phantom.

The inset in Fig. 4 presents the schematics of the dorsal skin flap model (CD-1 mouse). The mouse was anesthetized using isoflurane gas and the hair of the dorsal skin was shaved to expose the skin. We pinched the dorsal skin ( $\sim 1.5$  mm thick, scattering coefficient and anisotropy constant of  $\sim 8$  mm $^{-1}$  and  $\sim 0.8$ , respectively, for a 488-nm light source [19,20]) with two acrylic plates and applied a pressure of  $\sim 5$  psi (as measured by Prescale, Fujifilm) with four screws holding the plates in place. We selected the pressure level so that it would be sufficiently higher than the animal's blood pressure ( $\sim 2$  psi) [21].

#### 4.2. Result

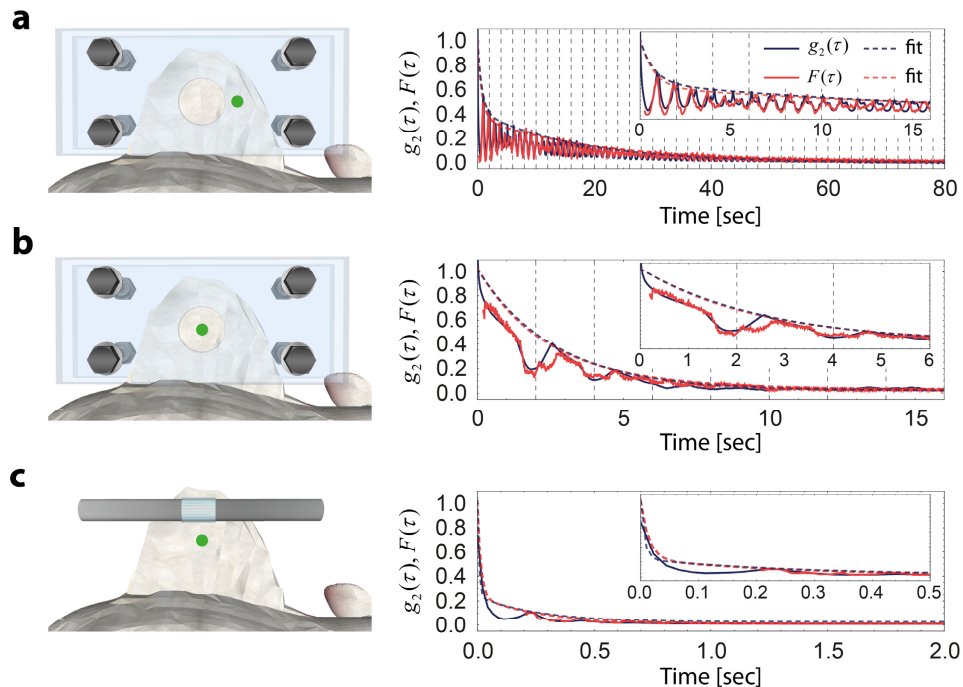


Fig. 5. Speckle intensity autocorrelation function and turbidity suppression fidelity measured through a mouse's dorsal skin flap. The solid lines (blue: speckle autocorrelation function, red: turbidity suppression fidelity) present the measured data and the dotted lines present two term exponential fit curves. The decorrelation characteristic time is determined as the time in which the fit curve drops to  $1/e$ . (a) Because the dorsal skin is significantly immobilized (directly pinched with pressure of  $\sim 5$  psi), both the autocorrelation function and the OPC turbidity suppression fidelity decrease slowly. The decorrelation characteristic time is around 2 s. The periodic oscillation of the signal is caused by respiratory movement. (b) When only the surrounding region is pinched (the laser beam is incident on the clear hole), the decorrelation characteristic time is only slightly changed. However, the autocorrelation function and the OPC spot intensity is not observed after  $\sim 10$  s. (c) Finally, if the skin is unclamped (tip of skin is glued to a rod) and is not immobilized by any physical means, the decorrelation characteristic time is decreased to  $\sim 50$  ms. For all three cases, we observed a high level of agreement between the speckle intensity autocorrelation and the turbidity suppression fidelity profile. 12 profiles were averaged to sample different breathing and heartbeat phases.

The decorrelation characteristic varied significantly depending on the degree of immobilization. Figure 5 shows the averaged data profile and fit profile. For all three cases,

the profile is oscillating because of the scatterers' movement caused from the heartbeat and breathing. We first find a local maximum for each data trace and fit the peak points to the two-term exponential function. The two-term exponential function is based on a simple physical model in which the dynamics of the scatterers are composed of a fast part and slow part [22]. The decorrelation characteristic time is determined as the time in which the fit curve drops to  $1/e$ .

When the skin was pinched directly, as in Fig. 5(a), the decorrelation characteristic time of both curves is approximately 2.5 s; however, considerable correlation between speckle ( $> 0.1$ ) patterns was observed until  $\sim 30$  s after the wavefront measurement step. The turbidity suppression fidelity followed a similar tendency. When the surrounding region was pinched as in Fig. 5(b), the characteristic time decrease does not change significantly. This implies that the scatterer dynamics is not significantly affected in the time scale of a few seconds even though the scatterer is less immobilized. However, the autocorrelation function and the OPC spot intensity drops to the noise level after  $\sim 10$  s. For the unclamped skin, the decorrelation characteristic time is reduced to  $\sim 50$  ms and the profiles drop to the noise level after  $\sim 1$  s (Fig. 5(c)). In Fig. 5(a) and 5(b), as the scatterers moved from and return to their original position due to breathing, the intensity autocorrelation function and the turbidity suppression fidelity oscillate along with breathing frequency of 0.5  $\sim$  1.0 Hz (which may vary depending on the anesthetization conditions [23]). For the mouse dorsal skin flap, the measurement of the OPC spot intensity is not synchronized with the measurement of the speckle intensity autocorrelation function. Instead, we measured twelve sets of two profiles (on the same part of the skin flap) in an alternating way and averaged the profiles (Fig. 5 (a)-5(c)). The starting time of each measurement is randomly chosen to sample different breathing and heartbeat phases. Again, we observed a good match of the two curves for all three cases. We note that the relative phase between the measurement and breathing (or heartbeat) only affects the shape of the oscillating profile but not the phase and frequency of it so that the peaks are still prominent in the averaged profiles.

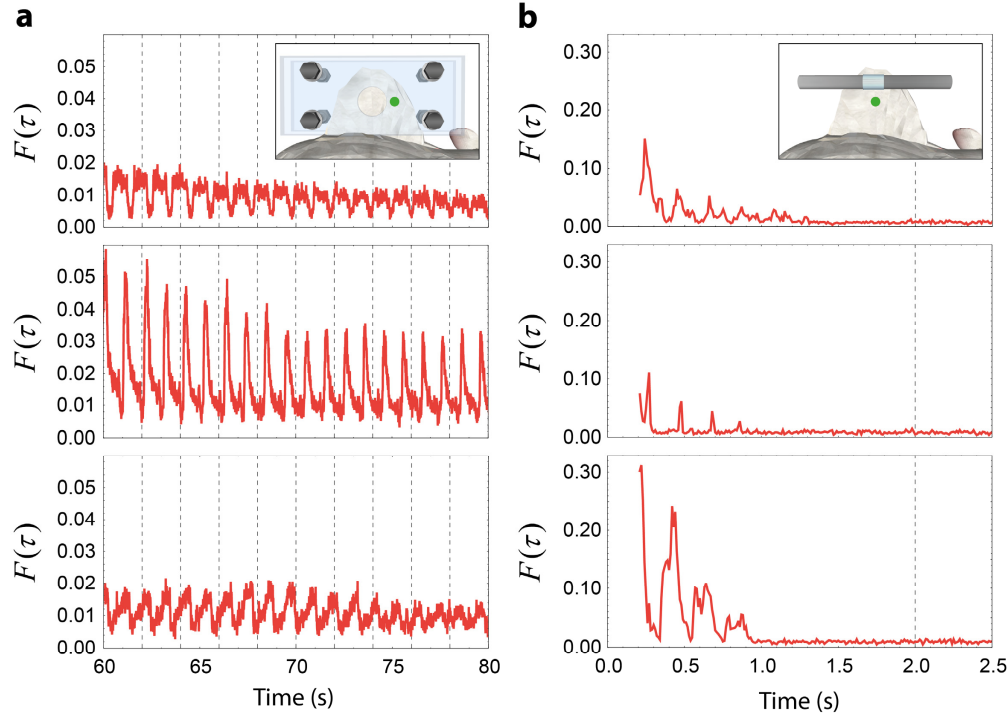


Fig. 6. Three typical time traces of the turbidity suppression fidelity (without averaging) in the low speckle intensity correlation regime. (a) The dorsal skin is pinched directly as in Fig. 5(a). (b) The dorsal skin is not immobilized as in Fig. 5(c). The shape of the profiles varies depending on the breathing and heartbeat phase.

In Fig. 6, we present the normalized OPC spot intensity in the low correlation regime without averaging (single data trace). Because the initial spot contrast was much greater than 1 (around  $10^4$ , shown in Fig. 7), we expected to observe the OPC spot even with the correlation below 5%. Figure 6(a) shows the case when the dorsal skin is directly pinched (Fig. 5(a)). The spot oscillating along with a breathing frequency could still be clearly seen after 60 s from the wavefront measurement. The spot decayed very slowly in this regime. We believe that this is because a portion of the scattered light passes through a relatively stationary portion of the tissue and this portion preserves the time-reversal symmetry. For the unclamped skin (Fig. 6(b)), the OPC spot also survived with a low speckle autocorrelation but the decorrelation characteristic time is much shorter than 1 s. It also shows the periodic oscillation with a frequency of about 5 Hz that is not easily seen in the averaged profile in Fig. 5(c). The frequency is consistent with the typical heart rate of an anesthetized mouse [23]. Because the oscillation at heartbeat frequency was not present in Fig. 6(a), we speculate that the oscillation observed through the unclamped skin originates from the pulsatory motion of the blood and vessels rather than from the whole-body movement caused by the heart beating. The main reason for the difference between the averaged profile and the single data profile is that each profile may change depending on the breathing and heartbeat phase when we record the OPC wavefront (Fig. 6).

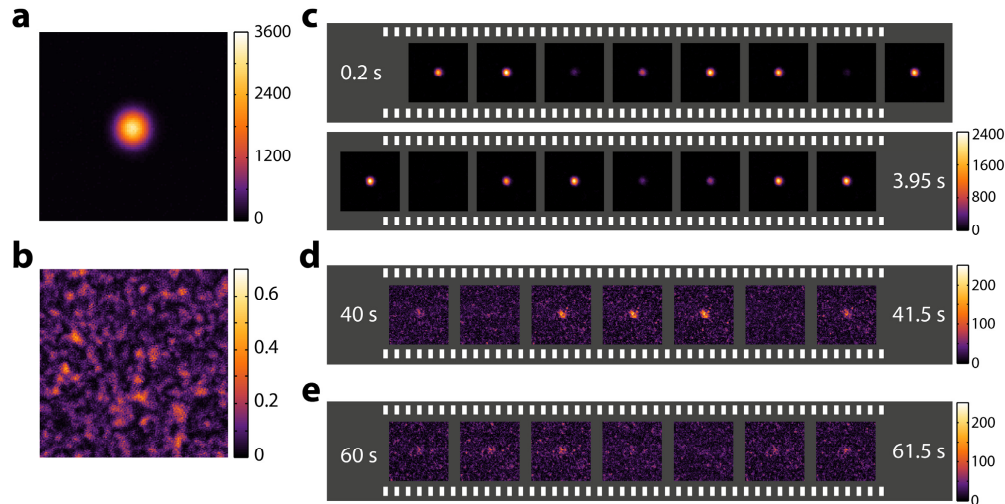


Fig. 7. (a) The OPC reconstructed spot and (b) the background measured through the dorsal skin of the euthanized mouse. (c-e) Time-lapse images of the OPC reconstructed spot captured 0.2 s, 40 s, 60 s after the OPC wavefront measurement. The spot decays over time and oscillates at the breathing frequency. The frame rate is around 4 Hz.

The reconstructed OPC spot is also observed on the CCD camera. Figure 7(a) and 7(b) show the reconstructed spot and background pattern captured through the dorsal skin of the euthanized mouse. The background intensity was measured after we shifted the pattern (OPC wavefront) displayed on the SLM by 100 pixels in both directions. The actual background signal was very low and dominated by ambient scattering light. We characterized the background intensity by averaging out many frames and subtracting the contribution from the ambient scattering. Figure 7(b) shows the background intensity after the subtraction of the experimental noise. The OPC spot contrast is estimated at  $\sim 10^4$  from the measured intensities.

In Fig. 7(c)-7(e), we present the time-lapse images of the OPC spot through the directly pinched dorsal skin. The starting time of each image sequence is 0.2 s (system latency), 40 s and 60 s after measuring the OPC wavefront. As measured from the APD, the spot decays over time and oscillates at the breathing frequency. The spot was observed after 60 s. Because the background in Fig. 7(c)-7(e) is dominated by the ambient scattering light, the spot contrast is not seen as high as expected. However, we note that the spot contrast should be estimated based on the properly measured background intensity (in Fig. 7(b)). For example, in Fig. 7(e), the spot contrast is  $\sim 300$  where the peak value is  $\sim 100$  and the averaged background intensity in Fig. 7(b) is  $\sim 0.3$ . This value is well matched with the turbidity suppression fidelity of  $\sim 3\%$ , which is measured from the APD.

## 5. Conclusion

We theoretically and experimentally investigated the relation between the speckle intensity autocorrelation function and the fidelity of the OPC turbidity suppression and found them to be equivalent. Based on this finding, we performed measurements through a live mouse dorsal skin flap ( $\sim 1.5$  mm thick) that underwent varying levels of immobilization. The decorrelation characteristic time ranged from 50 ms to 2.5 s. The high initial spot contrast ( $\sim 10^4$ ) naturally led to the survival of the spot at a low speckle autocorrelation. This implies that the OPC spot can survive for even longer when the initial spot contrast is high enough, which can simply be achieved by increasing the number of controllable optical modes (pixel number) in the DOPC system. This indicates the potential for using the OPC process for turbidity suppression of biological tissue because the feasibility of the OPC system can even be extended into the regime where the scatterer dynamics are much faster than the OPC system speed.

We also found that the decorrelation time changes significantly depending on the level of immobilization. When the dorsal skin flap was directly pinched, we expected the scatterer's movements caused by blood flow/pulsation and its fluidic environment to be significantly limited. However it resulted in the survival of the OPC spot for over 1 min, whereas the spot disappears in  $\sim 50$  ms for the unclamped dorsal skin. In other words, when tissue is immobilized, the stationary part of the tissue preserves the time-reversal property for a longer period. The characteristic time may vary depending on the thickness of tissue (number of scattering events), the type of tissue, and light collection geometry, as well as the level of immobilization. Interestingly, the unclamped skin presented a signal that oscillated along with heart rate while the immobilized (clamped) skin only presented oscillation along with the mouse's breathing rate. We believe that the heart rate oscillation is caused by a pulsatory motion involving blood and vessels that are limited by the pressure applied onto the dorsal skin. For practical biomedical applications, the wavefront at different phases of breathing and heartbeat may be averaged to create the non-oscillating OPC spot.

We optimized the DOPC system latency to  $\sim 200$  ms (with the auto-alignment method [14]) employing single-shot wavefront measurement (based on off-axis holography) and a fast computing unit. If a fast display device (e.g., a digital micromirror device) is utilized, the latency can be further shortened. We expect the one cycle of the DOPC procedure can be shortened by one order of magnitude if we optimize the data transfer time, memory read out time and display time. More specifically, the system operation time can be optimized in the following way. First the interferogram is directly transferred from the sensor to the field-programmable gate array (FPGA) board. Next the binarized wavefront of the signal beam is calculated on the board and transferred to the DMD control board. Finally the DMD displays the processed wavefront. Potentially, the integration of image sensor and spatial light modulator will also reduce the time required for the DOPC procedure [24]. Additionally, if more pixels (currently, around  $10^6$ ) are coordinated for the OPC process as indicated above, it seems highly probable that the OPC-based turbidity suppression technique may be applicable to highly dynamic biological tissue, such as brain tissue.

### **Acknowledgments**

This work is supported by NIH 1DP2OD007307-01 and a GIST-Caltech Research Collaboration grant and grants from the Institute of Medical System Engineering at GIST. Benjamin Judkewitz is the recipient of a Sir Henry Wellcome Fellowship from the Wellcome Trust. The authors thank Mr. Yeonsu Jung for help with in vivo experiments and theoretical development.